Three-Dimensional Physical Modeling of the Wet Manufacturing Process of Solid-State Battery Electrodes

Mohammed Alabdali[a], Franco M. Zanotto[a,b], Marc Duquesnoy[a,c], Anna-Katharina Hatz[d], Duancheng Ma[d], Jérémie Auvergniot[d], Virginie Viallet[a,b], Vincent Seznec[a,b,c], Alejandro A. Franco[a,b,c,e,*].

[a] Laboratoire de Réactivité et Chimie des Solides (LRCS), Université de Picardie Jules Verne, Hub de l'Energie, UMR CNRS 7314, 15 rue Baudelocque, 80039 Amiens, France
[b] Réseau sur le Stockage Electrochimique de l'Energie (RS2E), Hub de l'Energie, FR CNRS 3459, 15 rue Baudelocque, 80039 Amiens, France
[c] ALISTORE-European Research Institute, Hub de l'Energie, FR CNRS 3104, 15 rue Baudelocque, 80039 Amiens, France
[d] Umicore, 31 rue Marais, 1000 Brussels 8, Belgium
[e] Institut Universitaire de France, 103 boulevard Saint Michel, Paris 75005, France
* Author to whom any correspondence should be addressed: alejandro.franco@u-picardie.fr

Graphical Abstract

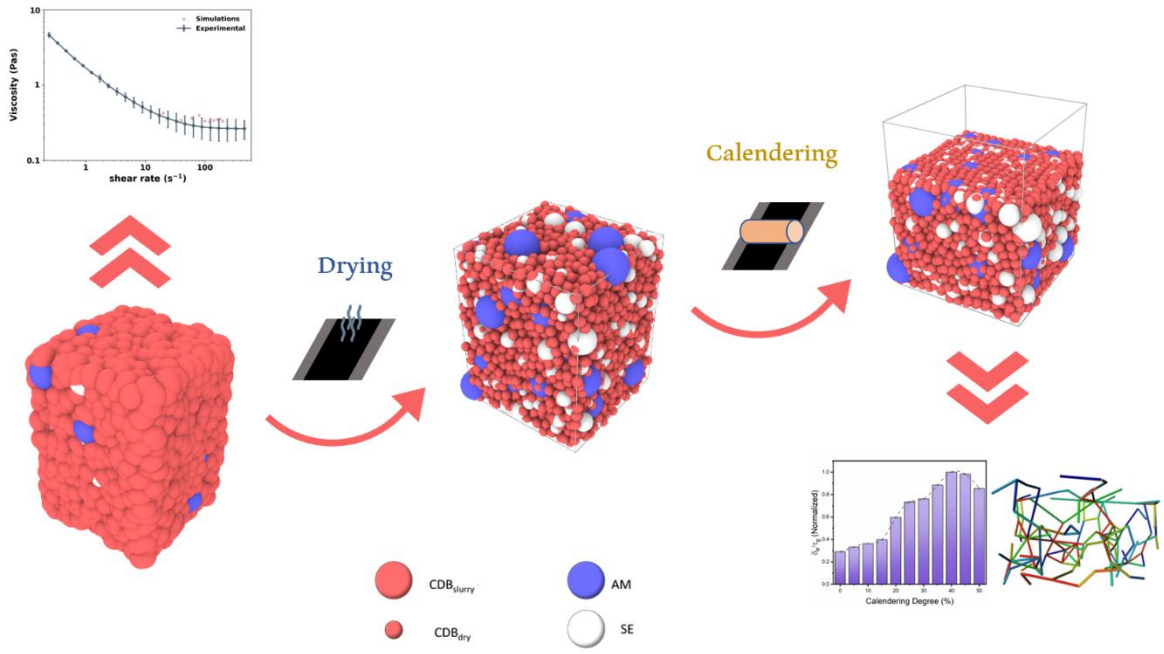

Abstract

Poor design of composite electrodes in Solid-State Batteries (SSBs) is one of the main reasons for their low performance. Although modeling techniques offer great potential in investigating multiple conditions for microstructure optimization, SSB manufacturing remains almost unaddressed in terms of computational studies. We present here a three-dimensional physics-based modeling workflow to investigate the impact of wet manufacturing process parameters on the properties of SSB tape casted composite electrodes based on $LiNi_{0.6}Mn_{0.2}Co_{0.2}O_2$ as the active material and Li_6PSCl_5 sulfide solid

electrolyte. Our proposed workflow models the entire process of wet manufacturing of SSB electrodes, starting with the slurry consisting of active material, carbon additive, binder, solid electrolyte and solvent, and continues through its drying process, and the calendering of the resulting electrodes. Our focus is in particular on the impact of the calendering degree on the microstructure of the electrode. We characterize the resulting microstructures in terms of electronic and ionic conduction properties. We believe that this first-of-its-kind wet manufacturing process model for SSB cathodes is an important step towards the development of systematic modeling approaches that can provide practical optimization of the interfaces between materials in electrodes to improve SSB performance and durability.

1. Introduction

Li-ion battery (LIB) is a technological breakthrough of high impact on modern society. Today, they are considered as the main enabler of the smartphone and electric vehicle industries [1], where the state-of-the-art LIB offers volumetric and gravimetric energy densities up to 770 $Wh.L^{-1}$ and 260 $Wh.kg^{-1}$ [2], respectively. LIBs are highly optimized and near their theoretical performance limits. Therefore, in the context of the increasing demand for energy coming from clean energy sources, a next generation of batteries with superior capabilities is needed to continue decreasing the energy grid's reliance on pollutant resources.

Solid-State Batteries (SSBs) use a solid electrolyte (SE) instead of a liquid electrolyte for the transport of Li ions. They are considered promising candidates for automotive applications since they are theoretically able to provide higher energy density and power performance than LIBs. Their high energy density originates from potentially enabling the use of a Li metal anode [3]. The SE layer prevents dendrite formation that causes short-circuits in Li-metal based LIBs. Due to poor electrode design[4], the performance of SSBs falls below that of the conventional LIBs even with superionic conductive solid electrolytes, *e.g.* the thiophosphates $Li_{5.5}PS_{4.5}Cl_{1.5}$[5] and $Li_{9.54}Si_{1.74}P_{1.44}S_{11.7}Cl_{0.3}$ [6] with ionic conductivity of 12 $mS.cm^{-1}$ and 25 $mS.cm^{-1}$, respectively. The performance of SSBs is heavily influenced by the electrode manufacturing process parameters such as the electrode composition and active material (AM) loading determine, *e.g*. the theoretical maximum capacity, internal resistance and the occurrence of parasitic (electro-)chemical reactions[7]. The mixing efficiency and densification during calendering in the electrode determine if the charge carriers can pass efficiently through the electrode, and whether a high utilization of cathode AM and efficient cycling at high C-rates can be achieved. Volume changes during processing and cycling may lead to contact loss and need to be considered to optimize the manufacturing process[4].

Even when high-capacity AMs, such as polycrystalline $LiNi_xMn_yCo_zO_2$ (NMC) and SE superionic conductors are used in SSB fabrication, they do not guarantee a highly performing SSB composite electrode. For instance, AM volume changes upon (de)lithiation raise various chemo-mechanical issues. One example is the cracking of polycrystalline $LiNi_{0.8}Mn_{0.1}Co_{0.1}O_2$ (NMC811) particles around 3.8 V[8,9], which leads to a loss of contact, since, unlike liquid electrolyte, the SE cannot access the new active surface areas within the pores created. It is recommended to use smaller particles such as single-crystalline NMCs to mitigate the risk of loss in contact due to particle cracking[10,11]. Another major challenge is the (electro-)chemical compatibility of the different materials within the composite electrode. The materials can decompose and form new interphases with new electronic and ionic properties heavily altering the performance of the electrode[12].

The development of composite electrodes is bottlenecked by the significant trade-off between achieving high energy density and fast charging rates. To achieve superior energy density, high utilization of AM and increased AM loading are required. This can be achieved by incorporating a high percentage of AM in the composite or through the use of additive carbon. However, a high AM fraction leads to a reduced percentage of SE and convoluted ion pathways. From an energy density perspective,

the presence of SE in the cathode is less desirable as it occupies space that could otherwise be used by the chemically active AM and high-density SEs, such as oxides or halides, adding significantly to the weight of the cell. In contrast, fast charging requires quick and short ion routes formed by a greater proportion of SE[13–15].

The manufacturing process of battery electrodes is a highly intricate and convoluted endeavor involving a series of sequential steps that are impacted by a wide range of parameters[16]. Deconstructing the influence of each of these manufacturing parameters on the output electrode microstructure and the resulting electrochemistry is challenging. To address this complexity, three-dimensional (3D) models have been developed by the ERC-funded ARTISTIC project[17], which serve as a powerful toolkit to investigate the impact of each parameter individually and in combination on the final electrode microstructure and electrochemistry. These tools are available online, with user-friendly interfaces, enabling users of all backgrounds to run simulations[18]. To accelerate the commercialization of SSBs, modeling can be leveraged as a fast and cost-effective testing strategy. It allows for a wide range of different assumptions to be explored in a relatively short time frame, in contrast, to slow and resource-intensive experiments. Modeling can provide valuable insights to improve every step in the SSB manufacturing process as well as to conduct advanced analysis and process control by providing real-time feedback and the ability to adjust manufacturing parameters on the fly, with the use of appropriate sensors in the production line[19].

3D physical models[20,21] of LIB electrode manufacturing have proven to show a good compromise between throughput and accuracy. Surprisingly, the available modeling literature on SSBs is less extensive[7] with a very limited number of studies focusing on manufacturing. LIB physics-based 3D models provide precise control for each of the manufacturing parameters enabling a high capability to understand and examine the effect of the manufacturing on the microstructure of the electrode. The output microstructure can be embedded into a heterogeneous 4D (time-dependent 3D) electrochemical model that links all of the manufacturing, microstructure and performance by ultimately predicting the experimental discharge curves from the initial set of manufacturing parameters. Our group has set up a series of LIB models attributed to different steps of the manufacturing process starting from the slurry phase[22], its drying[23,24], the dry electrode calendering[24,25] and electrolyte filling[26]. The final result of this model chain can be injected directly into 4D electrochemical models to simulate the energy discharge (current-potential curves)[27] and electrochemical impedance spectroscopy[28] for the resistance and conductivity of the electrode.

2. Materials and methods

2.1. Sample preparation and properties measurement

In order to prepare the slurry of the SSB composite electrode, the Li_6PS_5Cl (NEI) SE powder was pretreated via a wet ball milling process to reduce the size of the agglomerates. This treatment was determined based on an experimental study that employed machine learning to identify the optimal milling conditions for producing Li_6PS_5Cl SE thin films[29]. Wet ball milling experiments were conducted using a ball milling machine (Pulverisette 7, Fritsch) with 10 mm-diameter zirconia milling media and a zirconia jar in a dry room (dew point of -51 °C). P-xylene (≥ 99 %, Sigma-Aldrich) was mixed with Li_6PS_5Cl powder and then milled at 300 rpm for 2 hours. After milling, the mixture was left to dry overnight under vacuum at 80°C to obtain the wet milled SE (WM-SE) powder. Then, the particle size distribution (PSD) of the WM-SE was extracted from Scanning Electron Microscopy (Quanta 200F, FEI) images (Fig. S1).

The dry composite of the slurry was composed of $LiNi_{0.6}Mn_{0.2}Co_{0.2}O_2$ (NMC622, Umicore) AM, WM-SE and carbon additives (Super C45, MSE supplies) all of which were well mixed using mortar and pestle.

Additionally, the binder of styrene-butadiene-styrene copolymer (SBS, Sigma-Aldrich) was separately dissolved in the solvent p-xylene (≥99 %, Sigma-Aldrich) for 30 minutes at 70°C under continuous mixing. The solution was left to cool down to room temperature, then the dry composite was added to it and mixed in a standard laboratory vial at 800 rpm for one hour to formulate the slurry.

The viscosity of the slurry was determined by utilizing a rheometer (Kinexus lab+, Malvern Instruments) through the application of a shear rate range of 0.1 s^{-1} – 700 s^{-1}, resulting in the slurry's shear-viscosity curve. The slurry's density was measured by calculating the ratio between the slurry weight to the volume of the container.

The electrode composition and the PSD of the AM and SE are referred to as manufacturing parameters hereafter. The electrode composition is the weight fractions of the AM, SE, carbon additives and binder materials added while electrode fabrication. These manufacturing parameters have been previously tested and led to good results in terms of electrochemical performance and coating homogeneity. Throughout the simulation process, all manufacturing parameters were as experimentally defined and kept without further changes. The calibration of the Force Field (FF) parameters of the simulation outputs is done by comparison with the experiments after each manufacturing step.

2.2. Initial structure generation

Coarse-Grain Molecular Dynamics (CGMD) is a modeling technique employed to simulate the behavior of this system based on interactions among individual particles as beads presenting the materials (*i.e.* NMC622 AM, Carbon-Binder Domain (CBD) and Li_6PS_5Cl SE) involved in the wet manufacturing process, where the CBD is a geometrical domain within the model used to represent a phase consisting of the carbon additives, binder and in the slurry cases the solvent.

To initialize the simulation, particles of all materials need to be localized within the simulation box. In order to prevent the particles from overlapping at the initial stage, they are randomly generated within a large simulation box of 716 µm x 716 µm x 1000 µm dimensions. An isothermal-isobaric (NPT) condition at 300 K and 1 atm is applied, in which, the initial velocities of the particles are assigned in a random manner adhering to a distribution that corresponds to a temperature of 300 K.

2.3. Physical model development

To ensure proper initial generation of the particles and the equilibrium of the slurry the pressure and temperature are all set to 1 atm and 300 K, respectively, during the CGMD simulation. This is known as the NPT ensemble where particles, pressure, and temperature remain constant, which is maintained throughout the slurry and drying simulations. All simulations are carried out using LAMMPS[30].

The simulation is performed by solving Newton's equations of motion to output a 3D microstructure of SSB composite electrode in periodic boundary (PB) conditions. All of the three dimensions remain periodic during the simulation of each phase, except for the calendering process where just x and y dimensions are periodic since there is an applied pressure perpendicularly oriented to the z-axis. These conditions are applied to each manufacturing step (slurry, drying and calendering), with the output of the preceding phase being fed into the next as schemed in Fig. 1. This approach requires two sets of parameters: the manufacturing parameters, which determine the influence of each manufacturing process on the microstructure, and the FF parameters, which set the potential governing particles' interactions. The simulation workflow (Fig. 1) of the slurry, drying, and calendering take approximately 36, 96, and 24 hours, respectively, using one node with 128 GB of RAM and 2 processors (Intel® Xeon® CPU E5-2680 v4 @ 2.40 GHz, 14 cores) of MatriCS platform (Université de Picardie Jules Verne)[31].

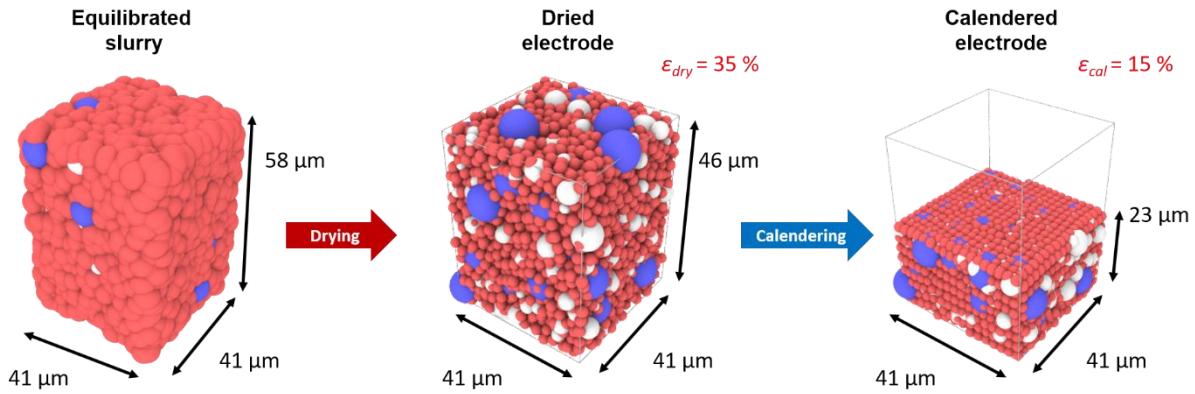

Fig. 1. Schematic of the CGMD-based modeling workflow of the slurry-based manufacturing process of an SSB composite cathode. It consists of three main manufacturing models: slurry, drying, and calendering. The blue beads stand for the AM, the white beads for the SE and the red beads for the CBD.

There are two FFs used to represent the physiochemical properties of the simulation whereas both FFs are available in LAMMPS simulation software[30]. The first FF is Lennard Jones (LJ)[32,33] which describes the interaction between a pair of simulated particles. The LJ FF is derived from the corresponding potential as expressed in Equations (1):

$$E_{LJ}(r) = 4\varepsilon\left[\left(\frac{\sigma}{r}\right)^{12} - \left(\frac{\sigma}{r}\right)^{6}\right] \quad r < r_c \tag{1}$$

E_{LJ} is LJ potential energy, where r is the distance between the center of two interacting particles, r_c is the cut-off distance at which there is no more interaction between the particles, ε is the depth of the potential well, more commonly known as dispersion energy and σ is the bond length. The other FF is Granular Hertzian (GH)[34,35] which represents the mechanical interactions of the granular media as illustrated in Equations (2):

$$F_{GH} = \sqrt{\theta}\sqrt{\frac{R_i R_j}{R_i + R_j}}\left[\left(k_{\mathrm{n}}\theta n_{ij} - m_{eff}\gamma_{\mathrm{n}}\mathrm{v}_{\mathrm{n}}\right) - \left(k_{\mathrm{t}}\Delta s_{\mathrm{t}} - m_{eff}\gamma_{\mathrm{t}}\mathrm{v}_{\mathrm{t}}\right)\right] \tag{2}$$

F_{GH} is the GH force, where R_i and R_j are the radius of two interacting particles, θ is the overlap distance, k_{n}, k_{t} are the elastic constants, γ_{n}, γ_{t} are viscoelastic damping constants and v_{n}, v_{t} are the relative velocity components between the two particles for the normal and tangential contact respectively. $m_{eff} = \frac{m_i m_j}{m_i + m_j}$ is the effective mass of both particles, Δs_{t} is the tangential displacement vector between the two interacting particles and n_{ij} is the unit vector that connects the centers of the two particles. The GH FF takes place when the two interacting particles, the experimental diameter of the AM and SE for the slurry model is increased by 14 % to account for the presence of the surrounding solvent[22] in the slurry step. Lastly, the friction coefficient is defined as the highest ratio between the normal and tangential forces which is expressed as: Xu, an additional GH parameter. All parameters for the FFs are listed in Table S1.

2.4. Conductivity and Tortuosity Calculation

We describe in this section the calculations to determine effective electronic conductivities (δ_e) and geometric tortuosity (τ_g). These were performed employing the DiffuDict and ConductoDict modules of GeoDict (Math2Market), using a standard desktop computer. The electrode's effective electronic

conductivity and the geometric tortuosity are two parameters chosen to have a quantitative indicator of the effect of the calendering degree on the electrode's electrochemical performance. They are simple observables defined to account for both ionic and electronic properties of the simulated dried (0 % calendering degree) and (5 % – 50 %) calendered electrodes. Herein, the calendering degree refers to the percentage of thickness reduction in the microstructure after calendering.

The microstructures' δ_e was calculated by solving the Poisson equation in the simulation domain, applying a 1 V potential difference between opposite sides along the z direction (perpendicular to the calendering plane). Then, Ohm's law is used to obtain the δ_e. The electronic conductivities of the AM and the CBD phases were set to 0.005 S m^{-1} and 15.93 S m^{-1} [36–38], respectively. PB conditions were considered for the outer xz and yz planes. The τ_g values were calculated according to $\tau = \sqrt{\frac{\eta}{D_{eff}}}$, where η is the volume fraction occupied by the SE and D_{eff} is the effective diffusion coefficient for Li ions in the SE medium. D_{eff} is in turn calculated by solving Fick's first law in the SE domain, with a concentration difference Δc between the outer xy planes. D_{eff} is obtained from the overall diffusive flux j as: $D_{eff} = -j \times length\ /\Delta c$. Since τ_g is only a geometrical magnitude, it is independent of the values chosen for Δc and the diffusion coefficient within the SE. Periodic boundary conditions were considered for the outer xz and yz planes.

3. Results and Discussion

3.1. Slurry CGMD Simulations

The CGMD simulations were conducted using LAMMPS software to model the three stages of the wet-based manufacturing process of 3D composite electrodes: slurry formulation, drying, and calendering. In our simulations, the particle beads are represented in the system as explicit different material types (*i.e.* NMC622 AM, SE and CBD), where CBD bead type is an effective particle that represents a blend of carbon, binder, and solvent in the workflow. The CBD diameter (d_{CBD}) and its density (ρ_{CBD}) account for effective parameters that are used for further optimization of the models and the physicochemical evaluation of the slurry simulation. The interaction between these particles was governed by FFs that were parameterized to match experimental properties, *i.e.* the experimental density, viscosity of the slurry and the porosity of the dry and calendered electrode. While the AM has a homogenous PSD of ~10 µm, the SE particles have sizes range 1 - 11 µm as shown in Fig S1. The simulation features a formulation for the dry composite of 69.0 % NMC622, 27.6 % LPSCl and 3.4 % CBD in the simulation and it includes 5089 particles in total. The CBD particles' diameter varied depending on the simulation stage. They have a diameter of 7.5 µm and a density of 0.9 g/cm^3 for the slurry and 3 µm for the dried electrode. We used the LJ and GH FFs available in LAMMPS software to model the entire manufacturing process. All input parameters for the LJ and GH FFs were calibrated to fit the experimental descriptors' output.

3.2. Slurry Viscosity fitting Simulations

The rheological properties of the slurry have a great impact on the manufacturing process[39–41]. The quality and speed of the coating, viscosity and the resulting cathode microstructure all depend on the slurry microstructure and its physicochemical properties. Many studies demonstrate the dependency of the final electrode characteristics (such as the structural and electrochemical properties) on the properties of the slurry [29,42].

Our computational workflow starts with the simulation of the slurry phase, so to calibrate the simulated microstructure, the density and viscosity as physical descriptors are compared to

experiments. The density is calculated at the end of slurry simulations by dividing the total mass of the particles by the volume of the simulated box. The viscosity of the simulated slurry model is calculated by a set of non-equilibrium CGMD (nE-CGMD) simulations performed to evaluate multiple shear viscosity values against the applied shear rates. To achieve this, the simulation box is deformed in one lateral direction by varying the angle of the x-y plane relative to the x direction. The deformation rate equals the chosen shear rate multiplied by the simulation box's length in the y direction. The results of this process are shown in Fig. 2, and the animation of the simulation is illustrated in a video in the supplementary materials. Additionally, sufficient time must be given for the simulation to converge towards its viscosity value. For this model, we used 7×10^7 timesteps of size $\Delta t = 0.001$ µs. The viscosity was obtained by averaging the instantaneous viscosity values after the convergence of the simulation. Each simulation took approximately two days using one node. The experimental density value of 1.90 g/cm^3 was used to validate the simulated slurry density of 1.89 g/cm^3.

To obtain FF parameters for the slurry model, Bayesian Optimization (BO) was initially conducted according to reference[43]. Bayesian multi-objective optimization was used to evaluate an objective function that was dependent on deterministic learning. To transform the multi-objective problem of fitting multiple FF parameters into a single objective function, we developed a scalarizing function. Gaussian Process regression was utilized as a model to approximate the value in each iteration, making BO an effective tool for multi-objective optimization. BO calculates posterior distribution over the set of all previous data and proposes new FF parameter values using an acquisition function that balances exploitation and exploration to identify nearby and far minima. The gaussian process model is updated at each step until the BO returns the optimal FF parameter values. By using this approach, we were able to identify the FF parameters that would produce good slurry density. After achieving a density sufficiently close to the experiments, it was improved by manual fitting for each of the FF parameters.

In the context of slurry coating, shear viscosity can provide valuable insights into the structural changes occurring within the slurry as it undergoes deformation due to applied stress. By studying the viscosity behavior, we can gain a better understanding of how the slurry's internal structure evolves during the coating process. From Fig. 2, it can be remarked that the results of the nE-CGMD viscosity simulations and the experimental observables demonstrate high agreement. Based on this agreement, the slurry model is considered to be well-fitted to serve as a digital representation, or a computational tool, for making further assumptions and predictions for the next steps of the process.

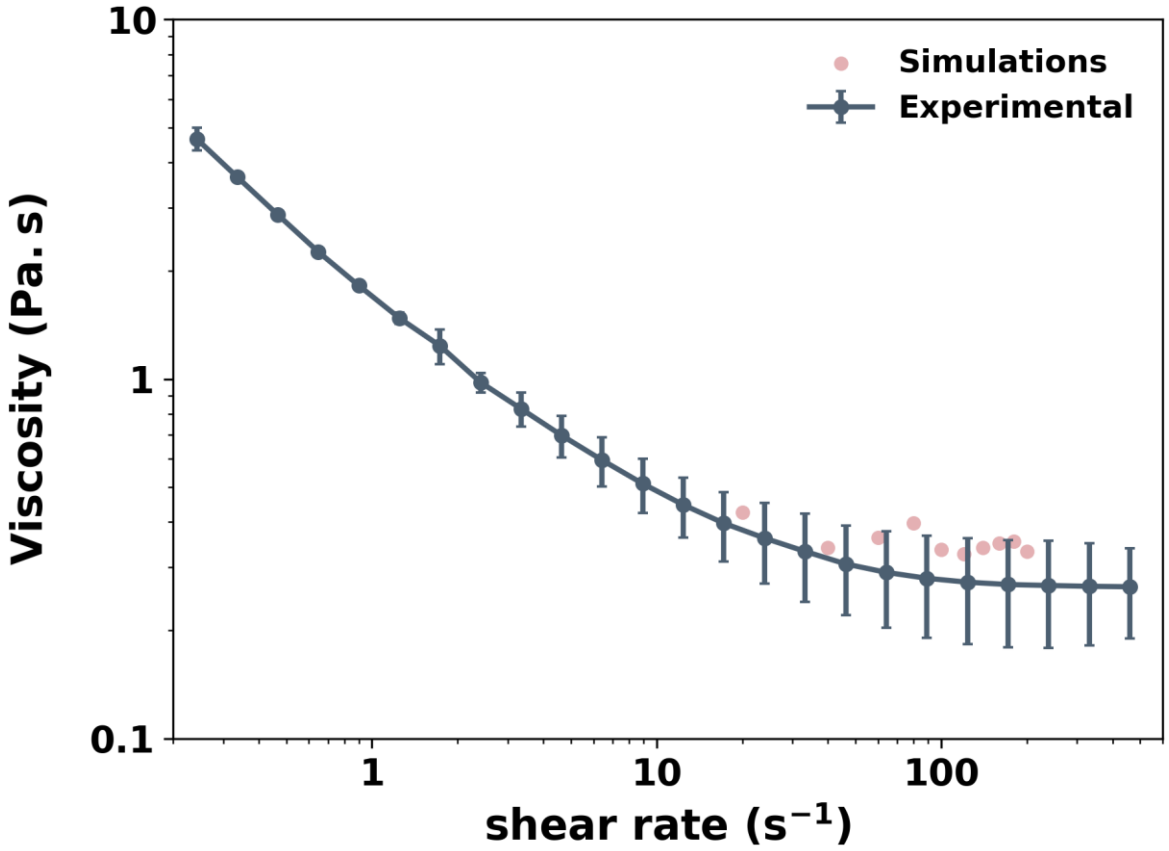

Fig. 2. Viscosity-shear rate curves obtained experimentally compared to the simulated results obtained via nE-CGMD.

3.3. Drying and Calendering CGMD Simulations

In the drying step, we adopt the homogeneous evaporation model[25] which assumes that all the 7.5 µm CBD particles containing the solvent will instantaneously shrink to the solid size of 3.0 µm, and then we allow the system to equilibrate. To imitate the phase changes from the slurry to the dried electrode, the FF parameters are adjusted by increasing the attractive and elastic interactions to account for stronger particle bonds due to binder bridges and the greater mechanical properties of the dry electrode. As a result, the electrode thickness decreases from top to bottom. At each time step, the temperature is maintained throughout the simulation at 300 K. We compare the simulation results with the experimental porosity[44,45], where both have a porosity of approx. 50 % assuming that the CBD phase comprises 50 % nanopores [46,47]. The degree of electrode compression is kept as an extra degree of freedom during calendering for further validation of the computational workflow to verify the simulated microstructures are sufficiently representative to undergo qualitative and semi-quantitative tests to find the impact of the calendering on the electrode by having different calendering degrees 0 % – 50 %.

Electrode calendering is a crucial process to enhance the electronic conductivity and mechanical strength of the electrodes, which are essential for optimizing the volumetric energy and power densities of battery cells. For SSBs, the objective is to obtain highly compact electrodes with the minimum porosity possible, resulting in an increase in ionic conductivity, rate capabilities, and utilization of the active material[4,48]. Therefore, analyzing the influence of calendering on the electrode microstructure is important to determine the optimal compression parameters that prevent

these issues. Our calendering model involves a plane moving downward at a constant speed to compress the electrode and simulate the actual calendering process. The interactions between the wall and the particles are governed by the GH FFs, where the forces between the wall and the particles depend on the same parameters described in Table S1. Throughout the calendering, the periodic boundary conditions are applied within the lateral x and y axes, while the surface perpendicular to the z-axis is maintained fixed. During the downward movement of the plane, the re-stabilization of the particles occurs due to self-organization.

Fig. 3a shows the porosity distribution along the electrode thickness. The porosity distribution decreases steadily with the evolution of the calendering, however, the electrode becomes highly compact under the high compression at 50 % calendering degree, where pores almost disappear. Fig. 3b and 3c demonstrate a comparison of the volume fraction of each material type along the electrode thickness. These figures show that the pores take a significant volume throughout the dry (0 % calendered) electrode with an even distribution of AM, SE and CBD. Due to the high pressure needed to reach 50 % calendering degree, the electrode becomes tightly compact. The pores and the CBD volume distribution drastically fall at the top of the electrode away from the current collector (CC), while the AM presence increases due to their larger particle size and superior mechanical properties. Finally, the SE model network (SENM) shown in Fig. 3d represents the complexity of the SE distribution within the electrodes, which reflects the evolution of the ionic pathways within the network of connected SE particles for various calendering degrees. Moreover, the pore network model (PNM) for all calendering degrees is displayed in SI, Fig. S4. As the pore size increases, the geometric tortuosity and volume of the SSB electrode also increase, negatively impacting both the power performance and energy density. Thus, the resulting microstructure's SENM and PNM were analyzed as a function of calendering degree using Avizo software (Thermo Fisher Scientific).

(a)

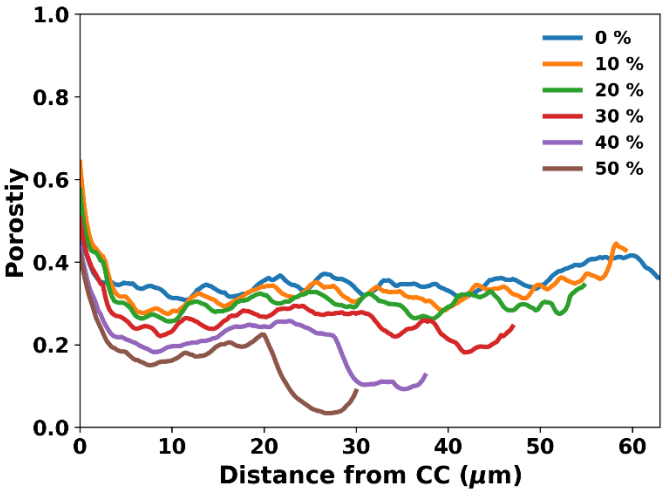

(b)

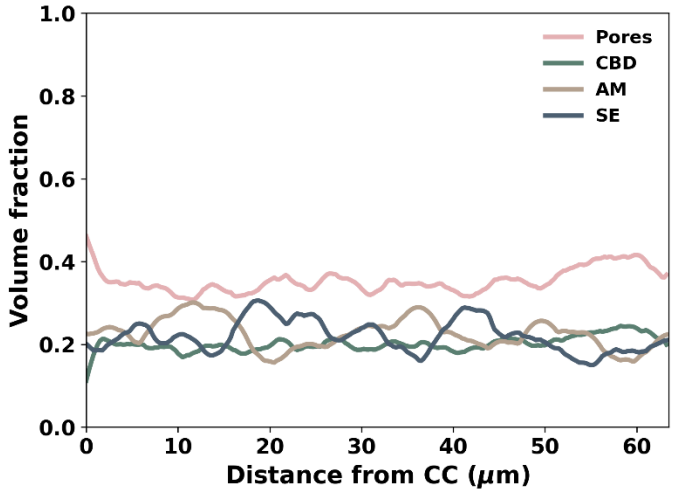
Pores
CBD
AM
SE
Volume fraction
1.0
0.8
0.6
0.4
0.2
0.0
0
10
20
30
40
50
60
Distance from CC (μm)

(c)

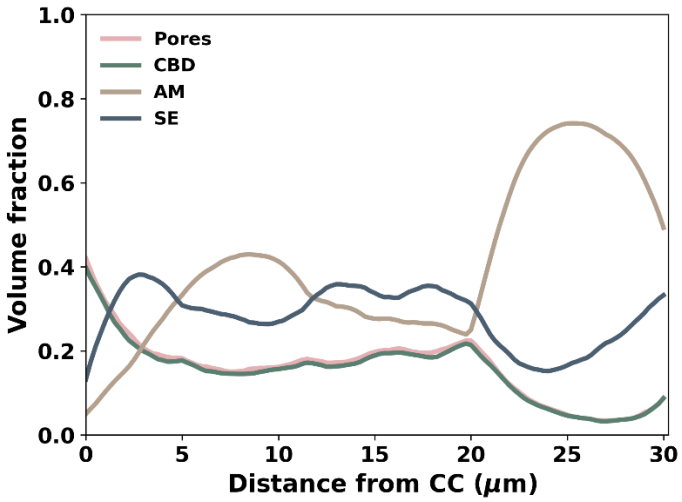
Pores
CBD
AM
SE
Volume fraction
1.0
0.8
0.6
0.4
0.2
0.0
0
5
10
15
20
25
30
Distance from CC (μm)

(d)

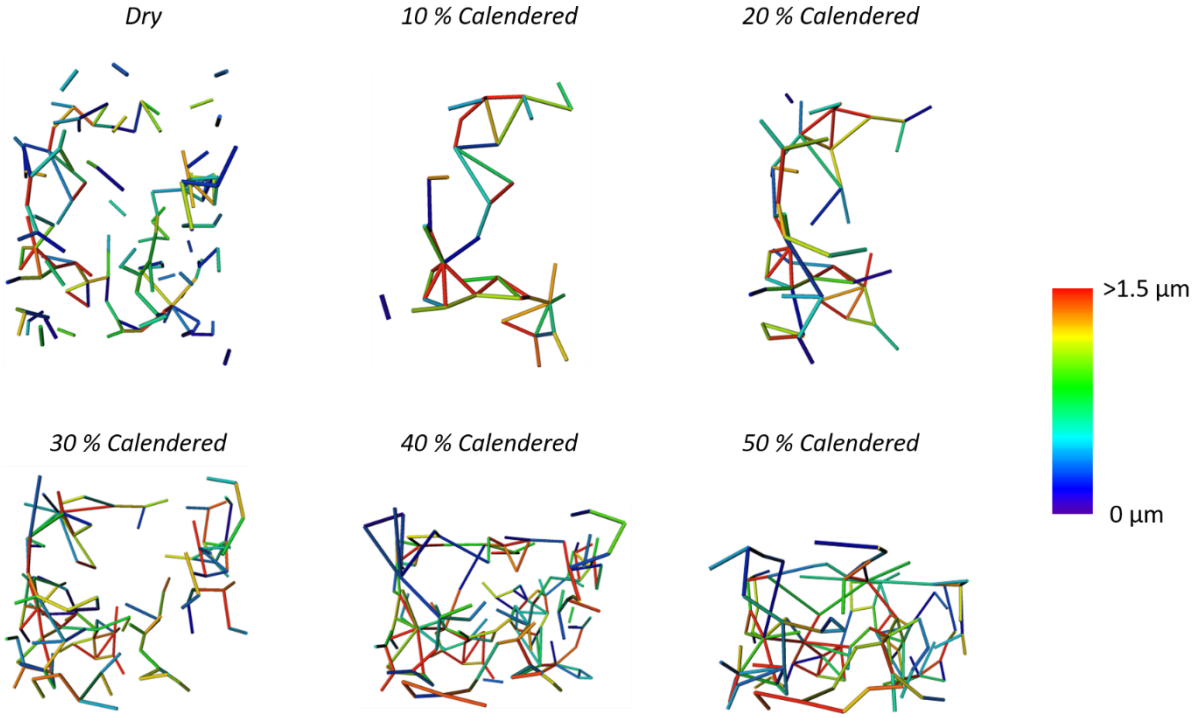

Fig. 3. (a) Evolution of the volume fraction of the porosity along the thickness of the resulting electrode microstructure under 0 % - 50 % calendering degrees (b) Volume fraction distribution along the thickness of the dry electrode microstructure. (c) Volume fraction distribution along the thickness of the 50 % calendered electrode microstructure (d) Evolution of the SENM of the resulting electrode microstructure under 0 % - 50 % calendering degrees.

3.4. Conductivity and Tortuosity Calculation

δ_e and τ_g were calculated using the DiffuDict and ConductoDict modules of GeoDict (Math2Market), as described in the Methodology section. These parameters were chosen to provide a quantitative indication of the effect of calendering degree on electrode electrochemical performance, accounting for both ionic and electronic properties of the simulated electrodes.

In the context of SSB the development of reliable electrochemical models is still in progress and currently not at the same level as the models for LIBs[7]. As an alternative approach, the evaluation of the conductivity and geometric tortuosity of the ion-conducting medium can serve as a preliminary indicator of the quality of the electrodes. By utilizing these parameters, it is possible to assess the optimal manufacturing conditions for achieving desired electrochemical performance.

Our approach of using δ_e and τ_g of the electronic and ionic conducting media as a general indication of electrode quality is particularly useful. Our results provide a quantitative means to evaluate manufacturing conditions and identify optimal calendering degrees for these electrodes. However, as the calendering degree increases from 0 % to 50 %, D_{eff} surges and τ_g plunges as shown in Fig. 4b, which is in agreement with the expected trend for improved electrode performance.

We observe in Fig. 4a an increase in δ_e that is consistent with the effect of higher compression on the electronic conductivity of the electrode. For the compression values, δ_e decreases. This observation is similar to our previous study on organic Na-ion batteries, where the δ_e started to decline after a certain calendering degree, yet the reason remained unstudied because of an experimental inaccessibility[49]. However, in Fig. 4a, the decrease in δ_e after 30 % can be attributed to the occupation of the volume of

CBD particles by other materials due to high pressure, which is a limitation shown by the model. Therefore, this model might be limited for calendering degrees under 35 %. This should be further investigated using different experimental and modeling approaches. However, we still observe a maximum in δ_e / τ_g values around 40 % (Fig. 4c).

(a)

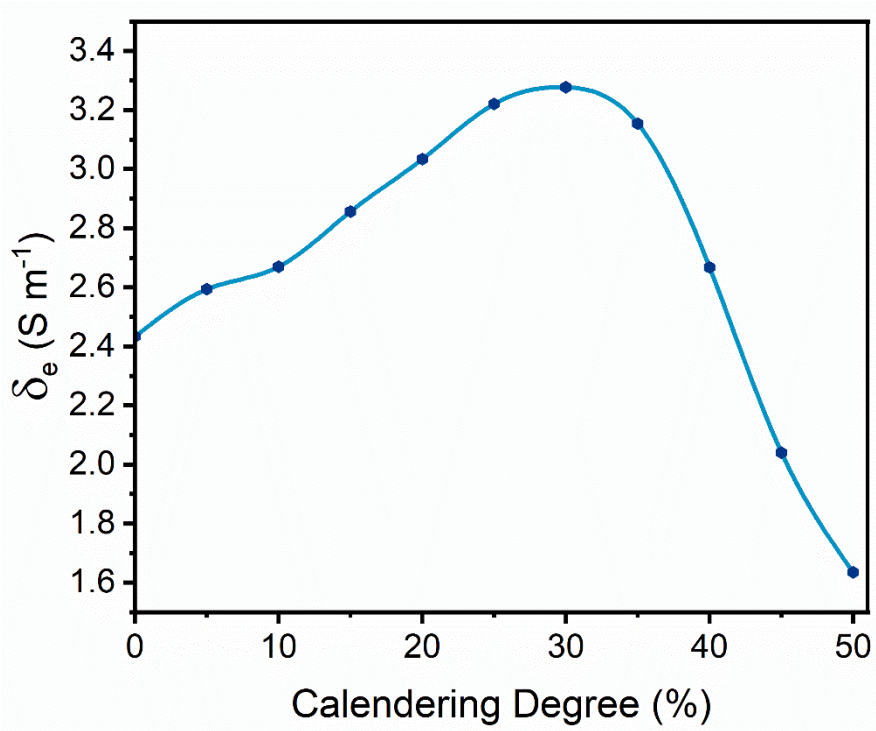

(b)

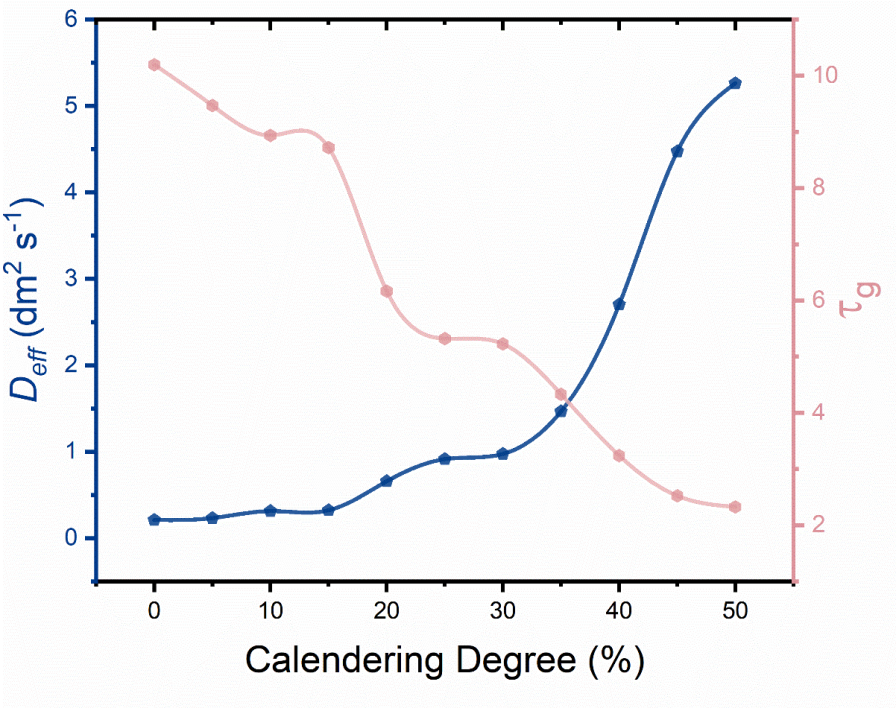

(c)

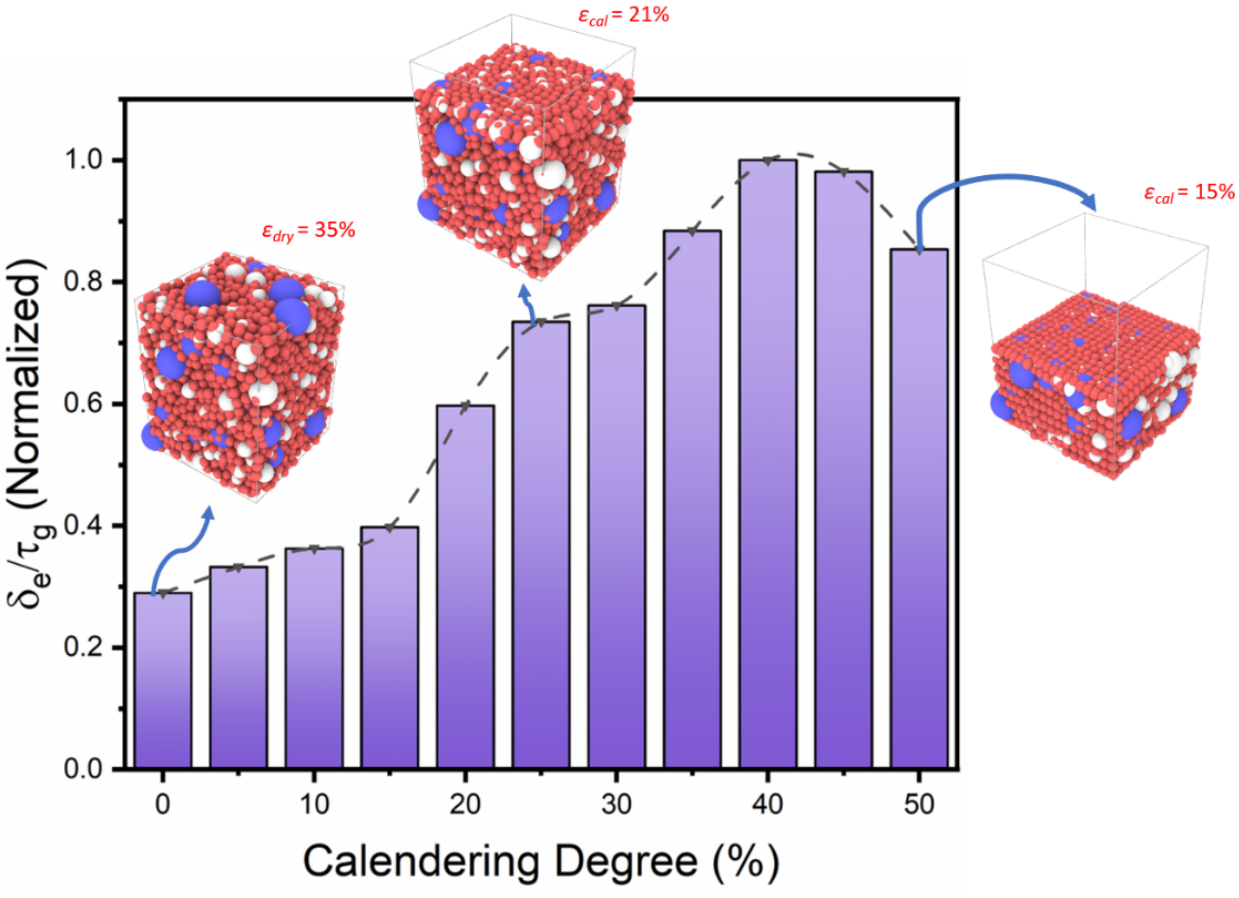

Fig. 4. (a) Electrode's effective electronic conductivity δ_e as a function of the calendering degree. (b) Electrode's geometric tortuosity $\boldsymbol{\tau_g}$ in blue and effective diffusion coefficient D_{eff} in red as a function of the electrode calendering degree. (c) Normalized ratio of the electrode's δ_e and $\boldsymbol{\tau_g}$ as a function of the calendering degree. The normalization is conducted by dividing by the maximum value.

4. Conclusion and Perspective

We present for the first time a physics-based computational workflow able to simulate in 3D the slurry-based manufacturing process of SSB composite electrodes using NMC622 as active material. The workflow has as inputs the materials and manufacturing process parameters. We use as an example here parameters identical to in our *in-house* experiments. It describes three major steps in the electrode wet manufacturing process: the slurry preparation, the drying and the calendering. This computational workflow, that was initially developed to simulate the manufacturing process of LIB electrodes, proved that is highly flexible to be extended and applied to diverse scenarios for a wide spectrum of electrochemical energy storage chemistries: LIB[24,25], SSB, Si/Gr[50] and organic Na-ion[49] batteries.

The simulation results are in excellent agreement with experimental data in regards of the slurry density, the slurry viscosity-shear rate curve, and the dried and the calendered electrode porosities[44,45]. The well-fitted simulation results demonstrate that this workflow consisting of several sequentially-coupled models is a good representation of the real wet manufacturing process to produce electrodes with similar features. Furthermore, the ratio between the electronic conductivity of the electrode to the geometric tortuosity is utilized as a quantitative descriptor to study the electrode microstructure under different degrees of calendering. The use of conductivity and geometric tortuosity of the ion conducting medium as indicators of electrode performance have provided valuable insights into the effect of calendering degree on SSB electrode performance. The analysis of this descriptor indicated an increase in the electrochemical performance with calendering. However, further research is needed to determine the optimal manufacturing conditions for SSB composite electrodes.

This work further demonstrates the chemical neutrality nature of the ARTISTIC project electrode manufacturing models [18,25,47,49], which are not limited to one type of electrochemical energy storage system, yet it can be extended to encompass the implementation of next-generation battery manufacturing. These experimentally validated computational procedures give the opportunity of inspecting a large number of combinations of the manufacturing parameters to rapidly examine the accuracy of assumptions before starting experiments. This is further amplified by the possibility of including machine learning tools in the workflow for the electrodes' optimization and the inverse design of the manufacturing parameters[43]. These models can be powerful in aiding the design and manufacturing of next-generation batteries that will help to rely on more sustainable energy sources with environmentally friendly properties.

5. Acknowledgments

M.A, V.S. and A.A.F. acknowledge the support by Umicore within the DESTINY PhD Programme, which has received funding from European Union's Horizon2020 research and innovation programme under the Marie Skłodowska-Curie Actions COFUND (Grant Agreement #945357). A.A.F. acknowledges the European Union's Horizon 2020 research and innovation program for the funding support through the European Research Council (grant agreement 772873, "ARTISTIC" project). A.A.F. and F.M.Z. acknowledge the European Union's Horizon Europe research and innovation programme under grant agreement No. 101069686 (PULSELiON). M.D. and A.A.F acknowledge the ALISTORE European Research Institute for funding support. A.A.F. acknowledges Institut Universitaire de France for the support.

6. References

[1] J.L. Brédas, J.M. Buriak, F. Caruso, K.S. Choi, B.A. Korgel, M.R. Palacín, K. Persson, E. Reichmanis, F. Schüth, R. Seshadri, M.D. Ward, An Electrifying Choice for the 2019 Chemistry Nobel Prize: Goodenough, Whittingham, and Yoshino, Chemistry of Materials. 31 (2019) 8577–8581. https://doi.org/10.1021/ACS.CHEMMATER.9B04345/.

[2] J. Janek, W.G. Zeier, A solid future for battery development, Nature Energy 2016 1:9. 1 (2016) 1–4. https://doi.org/10.1038/nenergy.2016.141.

[3] K.B. Hatzell, X.C. Chen, C.L. Cobb, N.P. Dasgupta, M.B. Dixit, L.E. Marbella, M.T. McDowell, P.P. Mukherjee, A. Verma, V. Viswanathan, A.S. Westover, W.G. Zeier, Challenges in Lithium Metal Anodes for Solid-State Batteries, ACS Energy Lett. 5 (2020) 922–934. https://doi.org/10.1021/ACSENERGYLETT.9B02668.

[4] A. Bielefeld, D.A. Weber, R. Rueß, V. Glavas, J. Janek, Influence of Lithium Ion Kinetics, Particle Morphology and Voids on the Electrochemical Performance of Composite Cathodes for All-Solid-State Batteries, J Electrochem Soc. 169 (2022) 020539. https://doi.org/10.1149/1945-7111/ac50df.

[5] P. Adeli, J.D. Bazak, K.H. Park, I. Kochetkov, A. Huq, G.R. Goward, L.F. Nazar, Boosting Solid-State Diffusivity and Conductivity in Lithium Superionic Argyrodites by Halide Substitution, Angewandte Chemie - International Edition. 58 (2019) 8681–8686. https://doi.org/10.1002/anie.201814222.

[6] Y. Kato, S. Hori, T. Saito, K. Suzuki, M. Hirayama, A. Mitsui, M. Yonemura, H. Iba, R. Kanno, High-power all-solid-state batteries using sulfide superionic conductors, Nat Energy. 1 (2016). https://doi.org/10.1038/nenergy.2016.30.

[7] M. Alabdali, F.M. Zanotto, V. Viallet, V. Seznec, A.A. Franco, Microstructurally resolved modeling of all solid-state batteries: Latest progresses, opportunities, and challenges, Curr Opin Electrochem. 36 (2022). https://doi.org/10.1016/J.COELEC.2022.101127.

[8] R. Ruess, S. Schweidler, H. Hemmelmann, G. Conforto, A. Bielefeld, D.A. Weber, J. Sann, M.T. Elm, J. Janek, Influence of NCM Particle Cracking on Kinetics of Lithium-Ion Batteries with Liquid or Solid Electrolyte, J Electrochem Soc. 167 (2020) 100532. https://doi.org/10.1149/1945-7111/AB9A2C.

[9] E. Trevisanello, R. Ruess, G. Conforto, F.H. Richter, J. Janek, Polycrystalline and Single Crystalline NCM Cathode Materials—Quantifying Particle Cracking, Active Surface Area, and Lithium Diffusion, Adv Energy Mater. 11 (2021). https://doi.org/10.1002/AENM.202003400.

[10] X. Li, Z. Ren, M. Norouzi Banis, S. Deng, Y. Zhao, Q. Sun, C. Wang, X. Yang, W. Li, J. Liang, X. Li, Y. Sun, K. Adair, R. Li, Y. Hu, T.K. Sham, H. Huang, L. Zhang, S. Lu, J. Luo, X. Sun, Unravelling the Chemistry and Microstructure Evolution of a Cathodic Interface in Sulfide-Based All-Solid-State Li-Ion Batteries, ACS Energy Lett. 4 (2019) 2480–2488. https://doi.org/10.1021/ACSENERGYLETT.9B01676.

[11] R. Fantin, E. Trevisanello, R. Ruess, A. Pokle, G. Conforto, F.H. Richter, K. Volz, J. Janek, Synthesis and Postprocessing of Single-Crystalline LiNi0.8Co0.15Al0.05O2 for Solid-State Lithium-Ion Batteries with High Capacity and Long Cycling Stability, Chemistry of Materials. 33 (2021) 2624–2634. https://doi.org/10.1021/ACS.CHEMMATER.1C00471.

[12] J. Janek, W.G. Zeier, Challenges in speeding up solid-state battery development, Nat Energy. 8 (2023) 230–240. https://doi.org/10.1038/s41560-023-01208-9.

[13] A. Bielefeld, D.A. Weber, J. Janek, Modeling Effective Ionic Conductivity and Binder Influence in Composite Cathodes for All-Solid-State Batteries, ACS Appl Mater Interfaces. 12 (2020) 12821–12833. https://doi.org/10.1021/ACSAMI.9B22788.

[14] Y.G. Lee, S. Fujiki, C. Jung, N. Suzuki, N. Yashiro, R. Omoda, D.S. Ko, T. Shiratsuchi, T. Sugimoto, S. Ryu, J.H. Ku, T. Watanabe, Y. Park, Y. Aihara, D. Im, I.T. Han, High-energy long-cycling all-solid-state lithium metal batteries enabled by silver–carbon composite anodes, Nat Energy. 5 (2020) 299–308. https://doi.org/10.1038/s41560-020-0575-z.

[15] P. Minnmann, L. Quillman, S. Burkhardt, F.H. Richter, J. Janek, Editors' Choice—Quantifying the Impact of Charge Transport Bottlenecks in Composite Cathodes of All-Solid-State Batteries, J Electrochem Soc. 168 (2021) 040537. https://doi.org/10.1149/1945-7111/abf8d7.

[16] Y. Liu, R. Zhang, J. Wang, Y. Wang, Current and future lithium-ion battery manufacturing, IScience. 24 (2021) 102332. https://doi.org/10.1016/J.ISCI.2021.102332.

[17] ERC Artistic : Home, https://www.erc-artistic.eu/ (accessed April 26, 2022).

[18] T. Lombardo, F. Caro, A.C. Ngandjong, J.B. Hoock, M. Duquesnoy, J.C. Delepine, A. Ponchelet, S. Doison, A.A. Franco, The ARTISTIC Online Calculator: Exploring the Impact of Lithium-Ion Battery Electrode Manufacturing Parameters Interactively Through Your Browser, Batter Supercaps. 5 (2022) e202100324. https://doi.org/10.1002/BATT.202100324.

[19] E. Ayerbe, M. Berecibar, S. Clark, A.A. Franco, J. Ruhland, Digitalization of Battery Manufacturing: Current Status, Challenges, and Opportunities, Adv Energy Mater. 12 (2022) 2102696. https://doi.org/10.1002/AENM.202102696.

[20] A.C. Ngandjong, A. Rucci, M. Maiza, G. Shukla, J. Vazquez-Arenas, A.A. Franco, Multiscale Simulation Platform Linking Lithium Ion Battery Electrode Fabrication Process with Performance at the Cell Level, Journal of Physical Chemistry Letters. 8 (2017) 5966–5972. https://doi.org/10.1021/ACS.JPCLETT.7B02647.

[21] A.A. Franco, A. Rucci, D. Brandell, C. Frayret, M. Gaberscek, P. Jankowski, P. Johansson, Boosting Rechargeable Batteries R&D by Multiscale Modeling: Myth or Reality?, Chem Rev. 119 (2019) 4569–4627. https://doi.org/10.1021/ACS.CHEMREV.8B00239.

[22] T. Lombardo, J.B. Hoock, E.N. Primo, A.C. Ngandjong, M. Duquesnoy, A.A. Franco, Accelerated Optimization Methods for Force-Field Parametrization in Battery Electrode Manufacturing Modeling, Batter Supercaps. 3 (2020) 721–730. https://doi.org/10.1002/BATT.202000049.

[23] A. Rucci, A.C. Ngandjong, E.N. Primo, M. Maiza, A.A. Franco, Tracking variabilities in the simulation of Lithium Ion Battery electrode fabrication and its impact on electrochemical performance, Electrochim Acta. 312 (2019) 168–178. https://doi.org/10.1016/J.ELECTACTA.2019.04.110.

[24] T. Lombardo, A.C. Ngandjong, A. Belhcen, A.A. Franco, Carbon-Binder Migration: A Three-Dimensional Drying Model for Lithium-ion Battery Electrodes, Energy Storage Mater. 43 (2021) 337–347. https://doi.org/10.1016/J.ENSM.2021.09.015.

[25] A.C. Ngandjong, T. Lombardo, E.N. Primo, M. Chouchane, A. Shodiev, O. Arcelus, A.A. Franco, Investigating electrode calendering and its impact on electrochemical performance by means of a new discrete element method model: Towards a digital twin of Li-Ion battery manufacturing, J Power Sources. 485 (2021) 229320. https://doi.org/10.1016/J.JPOWSOUR.2020.229320.

[26] A. Shodiev, E. Primo, O. Arcelus, M. Chouchane, M. Osenberg, A. Hilger, I. Manke, J. Li, A.A. Franco, Insight on electrolyte infiltration of lithium ion battery electrodes by means of a new three-dimensional-resolved lattice Boltzmann model, Energy Storage Mater. 38 (2021) 80–92. https://doi.org/10.1016/J.ENSM.2021.02.029.

[27] M. Chouchane, A. Rucci, T. Lombardo, A.C. Ngandjong, A.A. Franco, Lithium ion battery electrodes predicted from manufacturing simulations: Assessing the impact of the carbon-binder spatial location on the electrochemical performance, J Power Sources. 444 (2019) 227285. https://doi.org/10.1016/J.JPOWSOUR.2019.227285.

[28] A. Shodiev, E.N. Primo, M. Chouchane, T. Lombardo, A.C. Ngandjong, A. Rucci, A.A. Franco, 4D-resolved physical model for Electrochemical Impedance Spectroscopy of Li(Ni1-x-yMnxCoy)O2-based cathodes in symmetric cells: Consequences in tortuosity calculations, J Power Sources. 454 (2020) 227871. https://doi.org/10.1016/J.JPOWSOUR.2020.227871.

[29] Y.T. Chen, M. Duquesnoy, D.H.S. Tan, J.M. Doux, H. Yang, G. Deysher, P. Ridley, A.A. Franco, Y.S. Meng, Z. Chen, Fabrication of High-Quality Thin Solid-State Electrolyte Films Assisted by Machine Learning, ACS Energy Lett. 6 (2021) 1639–1648. https://doi.org/10.1021/ACSENERGYLETT.1C00332.

[30] LAMMPS Molecular Dynamics Simulator, https://www.lammps.org/ (accessed June 9, 2022).

[31] MatriCS Plateform – Shared platform for the research laboratories of the University of Picardie Jules Verne, https://www.matrics.u-picardie.fr/en/home/ (accessed March 24, 2023).

[32] pair_style lj/cut command — LAMMPS documentation, https://docs.lammps.org/pair_lj.html (accessed June 9, 2022).

[33] J.E. Lennard-Jones, Cohesion, Proceedings of the Physical Society. 43 (1931) 461–482. https://doi.org/10.1088/0959-5309/43/5/301.

[34] pair_style granular command — LAMMPS documentation, https://docs.lammps.org/pair_granular.html (accessed June 9, 2022).

[35] A.D.R. K. L. Johnson, K. Kendall, Surface energy and the contact of elastic solids, Proceedings of the Royal Society of London. A. Mathematical and Physical Sciences. 324 (1971) 301–313. https://doi.org/10.1098/rspa.1971.0141.

[36] R. Amin, Y.-M. Chiang, Characterization of Electronic and Ionic Transport in Li 1- x Ni 0.33 Mn 0.33 Co 0.33 O 2 (NMC 333) and Li 1- x Ni 0.50 Mn 0.20 Co 0.30 O 2 (NMC 523) as a Function of Li Content, J. Electrochem. Soc. 163 (2016) A1512–A1517. https://doi.org/10.1149/2.0131608jes.

[37] C. Liu, T. Lombardo, J. Xu, A.C. Ngandjong, A.A. Franco, An experimentally-validated 3D electrochemical model revealing electrode manufacturing parameters' effects on battery performance, Energy Storage Mater. 54 (2023) 156–163. https://doi.org/10.1016/j.ensm.2022.10.035.

[38] B.L. Trembacki, A.N. Mistry, D.R. Noble, M.E. Ferraro, P.P. Mukherjee, S.A. Roberts, Editors' Choice—Mesoscale Analysis of Conductive Binder Domain Morphology in Lithium-Ion Battery Electrodes, J. Electrochem. Soc. 165 (2018) E725–E736. https://doi.org/10.1149/2.0981813jes.

[39] K.B. Hatzell, M.B. Dixit, S.A. Berlinger, A.Z. Weber, Understanding inks for porous-electrode formation, J Mater Chem A Mater. 5 (2017) 20527–20533. https://doi.org/10.1039/C7TA07255D.

[40] W. Bauer, D. Nötzel, Rheological properties and stability of NMP based cathode slurries for lithium ion batteries, Ceram Int. 40 (2014) 4591–4598. https://doi.org/10.1016/J.CERAMINT.2013.08.137.

[41] G.W. Lee, J.H. Ryu, W. Han, K.H. Ahn, S.M. Oh, Effect of slurry preparation process on electrochemical performances of LiCoO2 composite electrode, J Power Sources. 195 (2010) 6049–6054. https://doi.org/10.1016/J.JPOWSOUR.2009.12.101.

[42] R.P. Cunha, T. Lombardo, E.N. Primo, A.A. Franco, Artificial Intelligence Investigation of NMC Cathode Manufacturing Parameters Interdependencies, Batter Supercaps. 3 (2020) 60–67. https://doi.org/10.1002/BATT.201900135.

[43] M. Duquesnoy, C. Liu, D.Z. Dominguez, V. Kumar, E. Ayerbe, A.A. Franco, Machine learning-assisted multi-objective optimization of battery manufacturing from synthetic data generated by physics-based simulations, Energy Storage Mater. 56 (2023) 50–61. https://doi.org/10.1016/j.ensm.2022.12.040.

[44] N. Riphaus, P. Strobl, B. Stiaszny, T. Zinkevich, M. Yavuz, J. Schnell, S. Indris, H.A. Gasteiger, S.J. Sedlmaier, Slurry-Based Processing of Solid Electrolytes: A Comparative Binder Study, J Electrochem Soc. 165 (2018) A3993–A3999. https://doi.org/10.1149/2.0961816JES/XML.

[45] T. Ates, M. Keller, J. Kulisch, T. Adermann, S. Passerini, Development of an all-solid-state lithium battery by slurry-coating procedures using a sulfidic electrolyte, Energy Storage Mater. 17 (2019) 204–210. https://doi.org/10.1016/J.ENSM.2018.11.011.

[46] L. Zielke, T. Hutzenlaub, D.R. Wheeler, C.W. Chao, I. Manke, A. Hilger, N. Paust, R. Zengerle, S. Thiele, Three-Phase Multiscale Modeling of a LiCoO2 Cathode: Combining the Advantages of FIB–SEM Imaging and X-Ray Tomography, Adv Energy Mater. 5 (2015) 1401612. https://doi.org/10.1002/AENM.201401612.

[47] J. Xu, A.C. Ngandjong, C. Liu, F.M. Zanotto, O. Arcelus, A. Demortière, A.A. Franco, Lithium ion battery electrode manufacturing model accounting for 3D realistic shapes of active material particles, J Power Sources. 554 (2023) 232294. https://doi.org/10.1016/J.JPOWSOUR.2022.232294.

[48] S. Li, Y. Sun, N. Li, W. Tong, X. Sun, C.T. Black, S. Hwang, Porosity Development at Li-Rich Layered Cathodes in All-Solid-State Battery during In Situ Delithiation, Nano Lett. 22 (2022) 4905–4911. https://doi.org/10.1021/acs.nanolett.2c01401.

[49] T. Lombardo, F. Lambert, R. Russo, F.M. Zanotto, C. Frayret, G. Toussaint, P. Stevens, M. Becuwe, A.A. Franco, Experimentally Validated Three-Dimensional Modeling of Organic-Based Sodium-Ion Battery Electrode Manufacturing, Batter Supercaps. (2022) e202200116. https://doi.org/10.1002/BATT.202200116.

[50] C. Liu, O. Arcelus, T. Lombardo, H. Oularbi, A.A. Franco, Towards a 3D-resolved model of Si/Graphite composite electrodes from manufacturing simulations, J Power Sources. 512 (2021) 230486. https://doi.org/10.1016/J.JPOWSOUR.2021.230486.

SUPPLEMENTAL INFORMATION

Three-Dimensional Physical Modeling of the Wet Manufacturing Process of Solid-State Battery Electrodes

Mohammed Alabdali [a], Franco M. Zanotto[a,b,], Marc Duquesnoy[a,c], Anna-Katharina Hatz[d], Duancheng Ma[d], Jérémie Auvergniot[d], Virginie Viallet[a,b], Vincent Seznec[a,b,c], Alejandro A. Franco[a,b,c,e,*].

[a] Laboratoire de Réactivité et Chimie des Solides (LRCS), Université de Picardie Jules Verne, Hub de l'Energie, UMR CNRS 7314, 15 rue Baudelocque, 80039 Amiens, France
[b] Réseau sur le Stockage Electrochimique de l'Energie (RS2E), Hub de l'Energie, FR CNRS 3459, 15 rue Baudelocque, 80039 Amiens, France
[c] ALISTORE-European Research Institute, Hub de l'Energie, FR CNRS 3104, 15 rue Baudelocque, 80039 Amiens, France
[d] Umicore, 31 rue Marais, 1000 Brussels 8, Belgium
[e] Institut Universitaire de France, 103 boulevard Saint Michel, Paris 75005, France
** Author to whom any correspondence should be addressed: alejandro.franco@u-picardie.fr*

S1. Scanning Electron Microscopy (SEM) images of the solid electrolyte (SE) before and after wet ball milling treatment

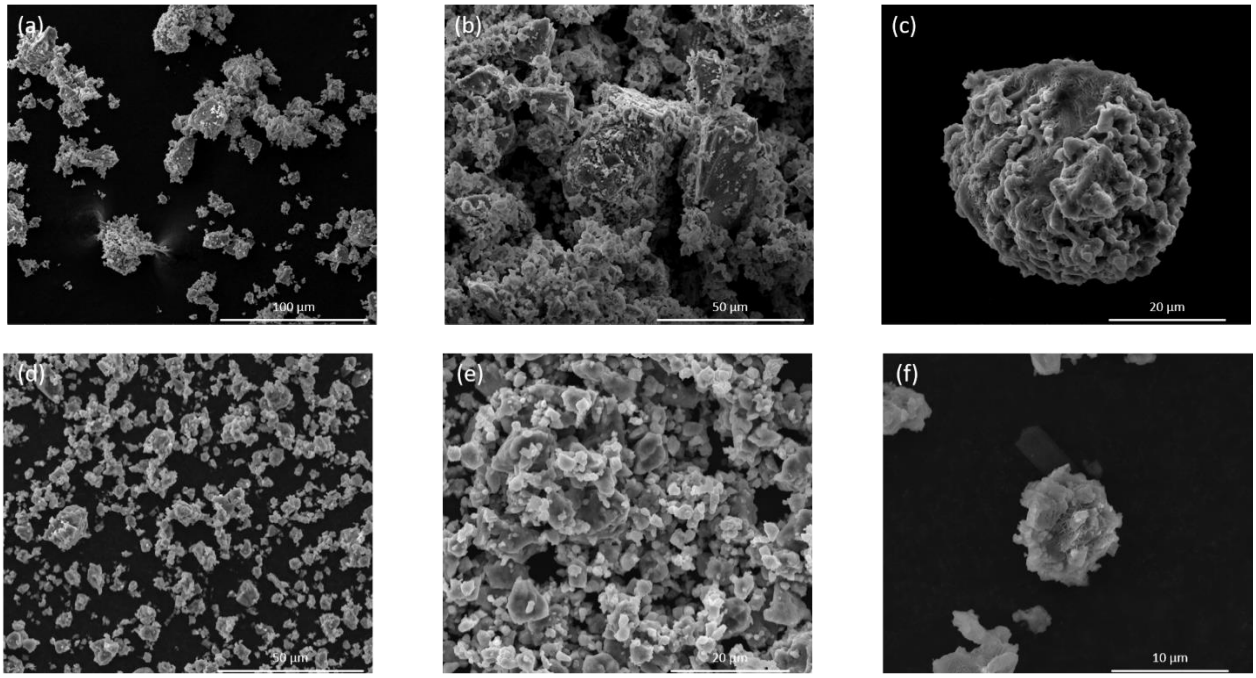

Fig. S1. (a), (b) and (c) Examples of SEM images of the commercial SE before wet ball milling treatment. (d), (e) and (f) Examples of SEM images of the wet ball milling treated SE used to measure the Particle Size Distribution.

S2. Particle Size Distribution (PSD) of the SE

The particle size distribution for the solid electrolyte was obtained from the SEM images above manually by measuring particle sizes (Fig S2a). A total of 2386 particles were measured to ensure representative results. This is later simplified to account for a smaller number of particle types in the modeling workflow (Fig S2b).

a)

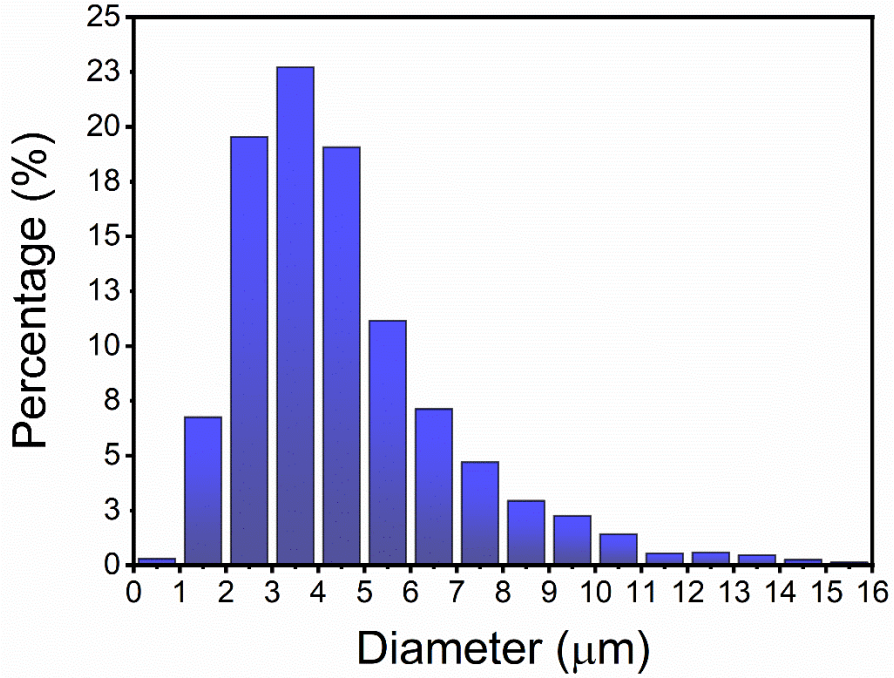

b)

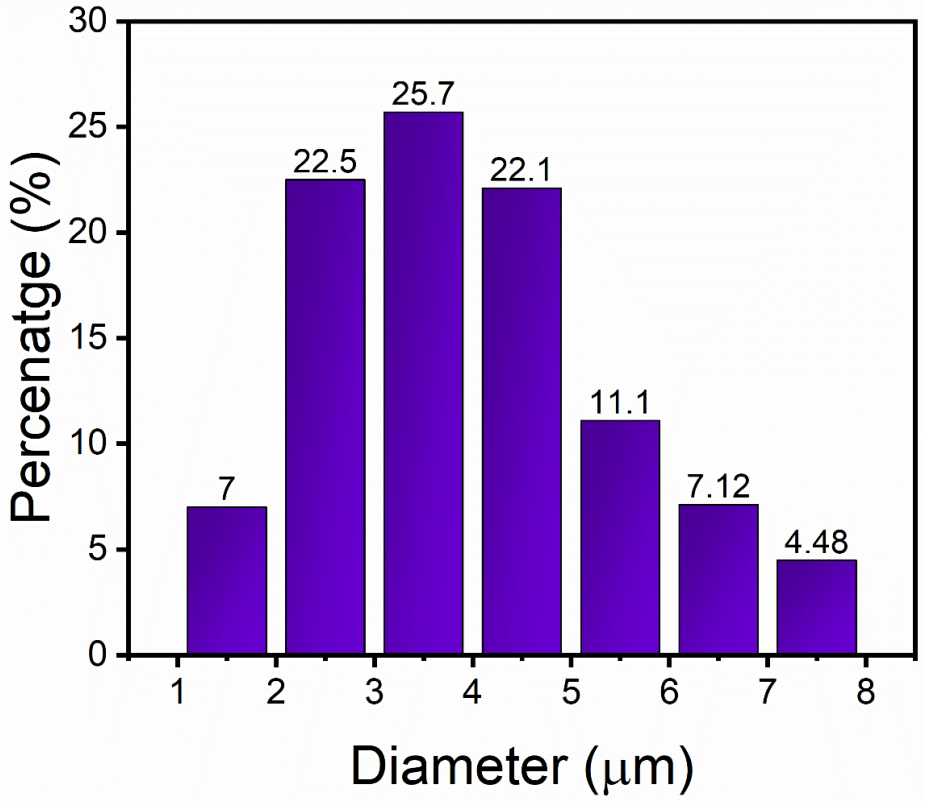

Fig. S2. a) The PSD of the SE collected from SEM images b) The PSD of the SE used in our simulations.

S3. Coarse-Grain Molecular Dynamics (CGMD) working principle

In general, molecular dynamics is a modeling technique which relies on force fields (FFs) to simulate the behavior of a system based on interactions among the individual particles. This simulation is performed by solving Newton's equations as function of these forces. CGMD[S1] represents the interactions between beads where each bead is a collective matter of atoms and/or molecules as a set of effective coarse-grained interactions. This allows for a more efficient simulation of the system as compared to traditional atomistic approaches, since the interactions between large groups of molecules are simplified to only a few parameters. In this way, CGMD offers the potential to simulate large systems of interacting molecules in a computationally efficient manner. In this work we consider the beads to be the NMC622 AM, the Li_6PS_5Cl SE and the CBD involved in the electrode wet manufacturing process, where the CBD is a geometrical domain within the model used to represent a phase consisting of the carbon additive, binder and the solvent in the case of the slurry (carbon additive and binder only in the cases of the dried and calendered electrodes).

S4. CGMD FFs

The LJ potential [S2, S3] is used for describing the interactions between pairs of particles. The principle of the Lennard-Jones potential assumes that the interaction energy between two particles can be described by a combination of a repulsive term, which is proportional to $(\frac{1}{r})^6$ where r is the distance (r) between the particles, and an attractive term, which is proportional to $(\frac{1}{r})^{12}$. The LJ Potential has three parameters: ε, σ and r_c. ε corresponds to the depth of the potential well, σ represents the distance at which the inter-particle potential is zero, and r_c is the distance at which the potential is truncated.

Granular Hertzian forces are a class of contact forces used to model the interaction between granular particles when they overlap [S2, S4]. The principle behind the Hertzian forces assumes that when two particles come into contact, the deformation of their surfaces can be described by a nonlinear elastic response. This response is characterized by a stiffness coefficient, known as the Hertzian modulus, which determines the force required to compress the particles together. The Hertzian forces have proven to be an effective way to model the behavior of granular materials, particularly under conditions of high strain rates or large deformations. The variables *kn*, *γn* and *Xu* correspond to the elastic constant and damping factor in the normal direction, and coefficient of friction, respectively. The ratio of the tangential to normal elastic constant and damping factor was determined as a function of the Poisson ratio, and these values were used to calculate the ratios *kt*/*kn* and *γt*/*γn*, which are 1.378 and 0.959, respectively.

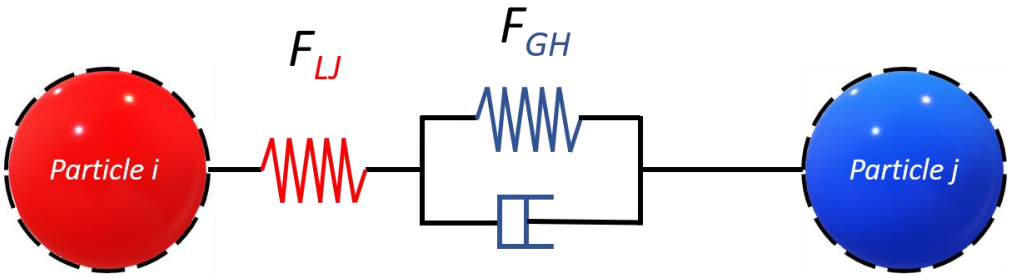

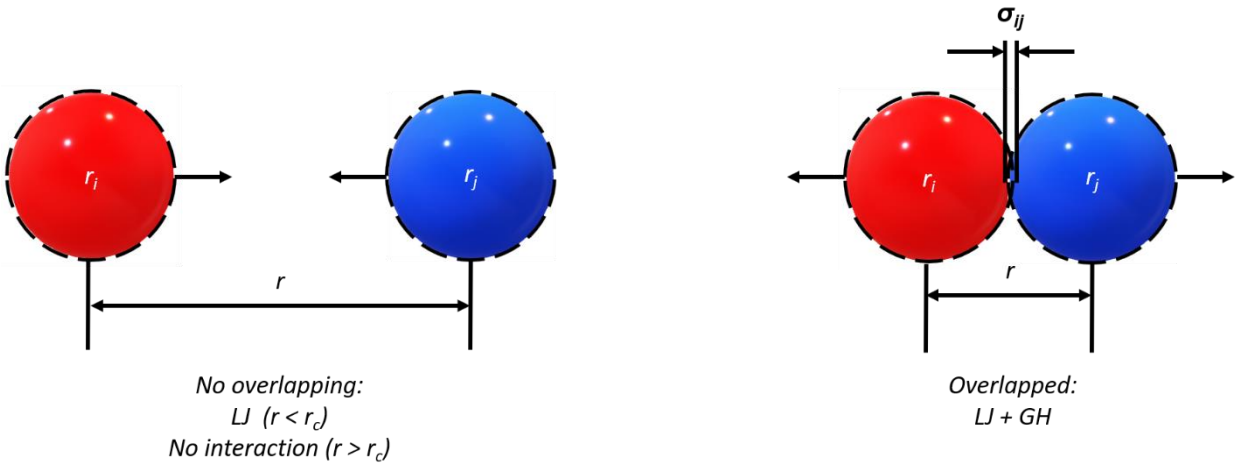

Fig. S3. Schematic representation of the applied FFs working principle in regard of the LJ and GH interactions between two particles within the CGMD simulations.

Table S1: The FF parameters values adopted in this work.

Parameters		Slurry	Dried electrode
LJ FF	ε_{CBD} [pg μm² μs⁻²]	0.88 × d_{CBD}	400 × d_{CBD}
	σ_{CBD} [μm]	0.97	0.89
	$r_{c\,CBD}$ [μm]	2.2 × d_{CBD}	2.2 × d_{CBD}
	ε_{AM} [pg μm² μs⁻²]	1.0 × d_{AM}	100 × d_{AM}
	σ_{AM} [μm]	0.99 × d_{AM}	0.93 × d_{AM}
	$r_{c\,AM}$ [μm]	1.5 × d_{AM}	1.2 × d_{AM}
	ε_{SE}[pg μm² μs⁻²]	10.5 × d_{SE}	200 × d_{SE}
	σ_{SE} [μm]	0.99 × d_{SE}	0.93 × d_{SE}
	$r_{c\,SE}$ [μm]	1.5 × d_{SE}	1.2 × d_{SE}
GH FF	k_n [pg μm⁻¹ μs⁻²]	0.1	100
	γ_n [μm⁻¹ μs⁻¹]	55	10
	X_u	0.016	12.5

7. S5. Pore Network Model (PNM) evolution

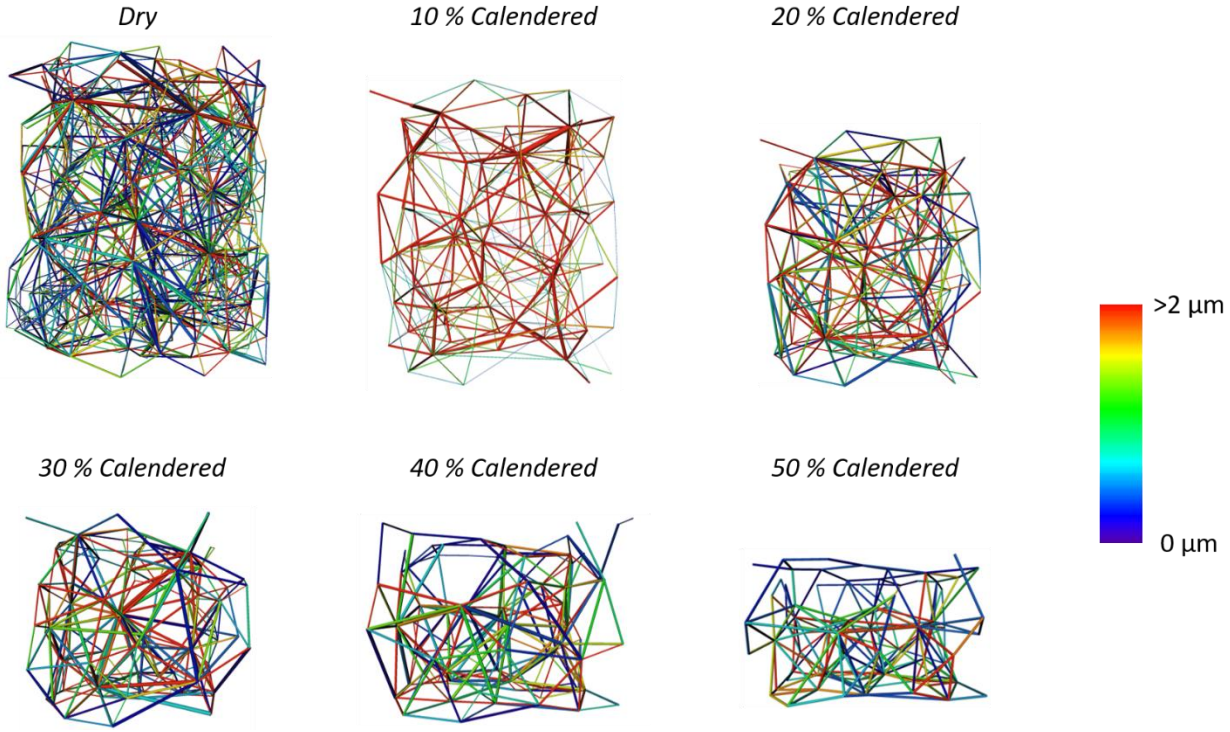

Fig. S4. Evolution of the PNM of the simulated electrode microstructure under calendering degrees 0 %-50 %.

8. S8. References

[S1] S. Kmiecik, D. Gront, M. Kolinski, L. Wieteska, A.E. Dawid, A. Kolinski, Coarse-Grained Protein Models and Their Applications, Chem Rev. 116 (2016) 7898–7936. https://doi.org/10.1021/acs.chemrev.6b00163.

[S2] T. Lombardo, J.B. Hoock, E.N. Primo, A.C. Ngandjong, M. Duquesnoy, A.A. Franco, Accelerated Optimization Methods for Force-Field Parametrization in Battery Electrode Manufacturing Modeling, Batter Supercaps. 3 (2020) 721–730. https://doi.org/10.1002/BATT.202000049.

[S3] J.E. Lennard-Jones, Cohesion, Proceedings of the Physical Society. 43 (1931) 461–482. https://doi.org/10.1088/0959-5309/43/5/301.

[S4] A.D.R. K. L. Johnson, K. Kendall, Surface energy and the contact of elastic solids, Proceedings of the Royal Society of London. A. Mathematical and Physical Sciences. 324 (1971) 301–313. https://doi.org/10.1098/rspa.1971.0141.